ARTICLE

Bismuth Drives the Morphology and Piezoresistivity of Lead-free $(TMSO)_3Sn_{3x}Bi_{2(1-x)}I_9$ Halide Perovskite thin films

Received 00th January 20xx,
Accepted 00th January 20xx

DOI: 10.1039/x0xx00000x

Simone Virga,[a]† Giuseppe Arrabito,[a]† Vittorio Ferrara,[a] Michelangelo Scopelliti,[a] Alessandro Longo,[b] Bruno Pignataro,*[a] and Francesco Giannici*[a]

The design of lead-free perovskite thin films with tunable optoelectronic properties is a hot topic in materials science, since it might enable the discovery of interesting properties outside the extensively explored field of photovoltaic solar cells. Herein, we report on the bending strain sensitivity of a lead-free hybrid organic-inorganic monodimensional iodide $(TMSO)_3Sn_{3x}Bi_{2(1-x)}I_9$ ($0 \le x \le 1$) showing complete miscibility of Bi^{3+} and Sn^{2+}, with TMSO being trimethylsulfoxonium. As previously shown in monodimensional haloplumbates, vacant cation sites are formed upon Bi^{3+} insertion, which in turn lead to the tunable shrinkage of the unit cell along the *a* axis. The effective substitution of Bi^{3+} and Sn^{2+} and their chemical state are investigated with EXAFS/XANES. Notably, Bi^{3+} also lowers the bandgap from 2.75 eV to 1.96 eV. Thin films prepared by spin coating on flexible ITO/PET supports are then used to assess the bending strain sensitivity as a function of composition, reaching an optimal value of the gauge factor (about 110 at 0.6% strain) at the highest Bi^{3+} concentration. The observed features are explained in terms of the surface morphology of the films as probed by AFM, highlighting the role of Bi^{3+}. The effects on microstructural and electrical features after strain are further investigated by SEM and EIS, underpinning the key role of microcracks and delamination for triggering the observed responsivity to bending strain.

Introduction

Halide perovskite-based materials are currently among the most extensively investigated materials for the fabrication of solar cells at high efficiency, since they can combine optimal optoelectronic properties and low-cost solution processability, allowing to reach efficiencies higher than 25%.[1] It is evident that these materials are playing a big role for the design of innovative technologies in the field of photovoltaics. Interestingly, they have also been widely explored in the field of optoelectronics for use as photodetectors,[2] diodes[3] and efficient energy harvesters based on piezoelectric $CsPbBr_3$ thin films.[4] Interestingly, the applications in the field of piezoelectricity and ferroelectric properties may be predicted by employing a high-throughput approach based on density functional theory allowing the correlation of the structural features to the electronic properties of these systems.[5] A benchmark in the field of piezoelectric perovskites is the $Pb(Ti,Zr)O_3$[6], resulting in its applications as piezoelectric actuator. In order to avoid lead in this class of ceramics, the Bi-based $BiFeO_3$ and $(Bi_{0.5}Na_{0.5})TiO_3$ perovskites have also been studied for their excellent piezoelectricity.[7] A recent example of lead-free piezoelectric perovskite[8] is the $0.3BaTiO_3–0.1Bi(Mg_{1/2}Ti_{1/2})O_3–0.6BiFeO_3$ ceramic, whose piezoelectric response is caused by the combinational partial ordering of the off-centered Bi ions that adapt their position under the application of an external electrical field.

In this scenario, halide perovskites have shown excellent piezoelectric and ferroelectric properties comparable to those of conventional inorganic piezoelectric materials.[9] For instance, the piezoelectric properties of hybrid methylammonium lead iodide $CH_3NH_3PbI_3$ thin films were studied by piezoelectric force microscopy,[10] with a piezoelectric coefficient $d_{33,eff}$ in the range of 6-25 pm/V under illumination. Other examples include the $CsPbBr_3$ thin films mentioned above,[4] and the two-dimensional hybrid perovskite

[a] Dipartimento di Fisica e Chimica "Emilio Segrè", Università degli Studi di Palermo, Viale delle Scienze, 90128 Palermo, Italy. E-mail: bruno.bignataro@unipa.it; francesco.giannici@unipa.it
[b] European Synchrotron Radiation Facility, 71, avenue des Martyrs, CS 40220, 38043 Grenoble Cedex 9, France and Consiglio Nazionale delle Ricerche, ISMN-CNR, I-90146 Palermo, Italy.
† These authors contributed equally to this work.
Electronic Supplementary Information (ESI) available: Rietveld refinements; optical spectra; electrical resistance after repeated bending; EIS fitting with different models. See DOI: 10.1039/x0xx00000x

ferroelectric (4-aminotetrahydropyran)$_2PbBr_4$ [(ATHP)$_2PbBr_4$].[11] Metal-free halide piezoelectrics with a perovskite structure have also been proposed recently,[12] based on MDABCO-NH_4-I_3 (MDABCO = *N*-methyl-*N*′-diazabicyclo[2.2.2]octonium)[13] or on NDABCO-NH_4-Br_3 (NDABCO = *N*-amino-*N*′-diazabicyclo[2.2.2]octonium) by replacing the methyl group of MDABCO with the amino group:[14] these show a d_{33} coefficient as high as 63 pC/N. To facilitate the applications into devices, perovskite halides crystals were also used as active fillers, e.g. $MAPbI_3$–polyvinylidene fluoride (PVDF) composite,[15] $CsPbCl_3$-PVDF reaching with $d_{33} \sim 49$ pm/V[16], and $CsPbBr_3$-poly(vinylidene fluoride–trifluoroethylene) with carbon nanotubes.[17]

The interplay of electrical and mechanical responses in halide perovskites is still far from being fully understood so that it can be fully implemented in real life strain sensors, and one major limitation is the difficulty in obtaining halide perovskite with good reproducibility and stability under ambient conditions. In this regard, piezoresistivity could represente an alternative piezo-based transduction mechanism, where the mechanical strain triggers changes in the electrical resistance or conductivity,[18] without generating a potential like in the piezoelectric transduction. Such effect is based on cracks or gaps among conductive domains within the material structure directly resulting from the application of strain. As a result, the variation of gap sizes or the shrinkage of the material conductive paths determines electrical resistance changes that can be quantified at ease by an external measuring circuit. However, piezoresistivity in halide perovskites is at present still underexplored, due to the well-known issues of instability when in contact with air.[19] To this aim, most works have focused so far on composites of halide nanoparticles dispersed in suitable polymer matrices to enhance their stability, ultimately providing flexible strain sensors, e.g. $MASnBrI_2$ nanocrystals in polyurethanes,[20] and $CsCuCl_3$ in PVDF.[21] To our knowledge, no studies exist on thin films hybrid piezoresistive halide perovskites that could facilitate the integration into sensor devices.

Here, we investigate the onset of previously unknown piezoresistive properties in lead-free hybrid organic-inorganic tin/bismuth iodides $(TMSO)_3Sn_{3x}Bi_{2(1-x)}I_9$ ($0 \leq x \leq 1$), where TMSO is the trimethylsulfoxonium cation. Although not perovskites in a strict sense, various lower-dimensional lattices of halometallates sharing vertices, edges or faces are (somewhat liberally) also called perovskites in recent literature, due to their broadly similar photophysical properties and crystal chemistry. The resulting hybrid perovskite shows the formation of vacant cation sites controlled by the concentration of Bi^{3+} cations, which induces a shrinkage of the crystalline cell along the a-axis. The perovskite structural chemistry is deeply investigated by using advanced X-ray based techniques. Thin films produced by spin coating onto ITO/PET supports show a dramatic variation of their morphological features and piezoresistive properties as a function of the Bi^{3+} content, ultimately finding an optimized value which is well correlated with the formation of vacant cation sites induced by the Bi ions. The physical and chemical properties of the thin films are extensively studied by surface-sensitive techniques,[22] such as X-ray photoelectron spectroscopy (XPS), scanning electron microscope (SEM), and atomic force microscopy (AFM), demonstrating the correlation between the concentration of Bi^{3+} concentration in the perovskite and the piezoresistive properties of the thin film. This work can constitute a first step towards the rational design of lead-free halide perovskite thin films with piezoresistive properties controllable by the concentration of Bi^{3+}.

Methods

Bulk powders: synthesis and characterization

Tin oxide (SnO, 99%, Alfa Aesar), bismuth oxide (Bi_2O_3, 99.9%, Sigma-Aldrich), hydroiodic acid (HI, 57% w/w aqueous stabilized with 1.5% H_3PO_2, Alfa Aesar), trimethylsulfoxonium iodide ($((CH_3)_3SO)I$, >98%, Alfa Aesar), were all used as received. All samples with general formula $(TMSO)_3Sn_{3x}Bi_{2(1-x)}I_9$ were synthetized through precipitation from aqueous solution as described in detail in our earlier work,[23,24] using SnO_2 instead of PbO_2.

X-ray diffraction (XRD) patterns were acquired on all samples with a Rigaku Miniflex 600 diffractometer using Ni-filtered Cu Kα radiation, and analyzed with Rietveld refinement using GSAS-II (Fig. S1-S5).[25] All samples were refined with an orthorhombic *Pnma* structure and all lattice parameters obtained from refining are given in Table 1.

X-ray absorption spectra were acquired at Bi L_3-edge and Sn K-edge at the BM8 beamline of ESRF (Grenoble, France). Spectra were acquired in transmission mode on samples cooled at 100 K with a liquid nitrogen cryostat. Each sample was measured on a grid of nine spots ca. 1 mm apart to minimize beam exposure, with each scan lasting about 40 min, and all scans averaged afterwards. For each sample, pellets were prepared by dilution with boron nitride. Data reduction was performed with Athena.[26]

X-ray Fluorescence Spectroscopy (XRF) was performed on the powders of the three mixed-metal phases were deposited on a polycarbonate film and analyzed with a MiniPal2 XRF spectrometer (PANalytical), working with a Cr anode at 30 kV and 3 µA, using an Ag filter. X-ray fluorescence lines were measured for Sn ($K\alpha_1$ line, at 25.2 keV) and Bi ($L\alpha_1$, $L\beta_1$ and $L\gamma_1$ lines, at 10.8, 13.0 and 15.2 keV, respectively). Intensity calibration was performed using an equimolar amount of Sn and Bi, using a $(TMSO)SnI_3$ and $(TMSO)_3Bi_2I_9$ mixture.

UV-vis-NIR reflectance spectra of the powder were measured in the 200-800 nm range using a Jasco V-770 spectrophotometer equipped with an integrating sphere. The Kubelka–Munk function F[R] was calculated from the reflectance spectrum, using the F[R] = (1 − R)2 / 2R relationship. Taking F[R] as the representative of the sample absorbance spectrum, extrapolation of the linear portion of the $(F[R]\ h\nu)^2$ vs. hν plot on the hν axis provided experimentally accessible direct band gap values (Tauc plots).

Thin films: deposition and characterization

Dimethylformamide (DMF, >99.8%, Sigma-Aldrich), isopropyl alcohol (C_3H_8O, >99.7%, Sigma-Aldrich), and absolute ethanol (C_2H_6O, 99.97%, VWR) were all used as received. Thin films were prepared by dissolving the powder with a concentration of 40 mg/mL in DMF, stirring the solution at 30 °C until a clear solution was obtained. The solution was filtered through 0.22 µm Millipore PTFE syringe filter. Then, 100 µL of solution were spin-coated for 20 s at 4000 rpm using an Ossila system on 1 mm-thick and 24 x 24 mm^2 ITO/PET substrates. Before film deposition, the substrates were sonicated in isopropyl alcohol for 10 min and treated in an ozone cleaner for 30 min.

Transmission mode UV–vis spectra were recorded with a Analytik Jena Specord S600 spectrophotometer in the range of 300–650 nm. All spectra were acquired on films deposited on 24 x 24 mm^2 glass substrates, using the latter as blank.

The electrical and impedance characterizations were conducted using a instrument Metrohm Autolab PGSTAT 128 N potentiostat/galvanostat. The electrical response of the sensors was acquired as current–potential (I–V) analyses with a two-electrode connection, linked to the two ends of the ITO 24 × 24 mm^2 active area, connected by crocodile clips. The sensing electrode (S) was short-circuited with the reference electrode (RE), to avoid Ohmic losses. The potential range used was from −2 to +2 V with a scanning speed equal to 0.1 V/s. The sensors were placed on a custom 3D-printed folding device, with a 10 mm sized curvature radius. The bending measurements were performed by affixing the sensors to Kapton tape at both ends. Specifically, one end was securely fixed with Kapton tape, while the other was adjusted to vary the angular position, corresponding to the sensor movement on the folding device. The samples were placed on the folding device, and their behavior was analyzed under static conditions at bending angles equal to 0°, 30°, 60°, and 90°. At each bending step, the folding device is elongated by approximately 5 mm. For each angle, 14 repeated measurements were performed on each sample. Electrochemical Impedance Spectroscopy (EIS) measurements were carried out in the frequency range comprised between 0.05 Hz and 500 kHz, using a sine wave at 10 mV potential and 0 V bias. The fit of the equivalent circuits from the EIS data was carried out with the Nova 2.1.5 software. Measurements of electrical resistance variations were acquired with a PeakTech 2025 multimeter.

X-ray Photolectron Spectroscopy (XPS) spectra of the deposited thin film were acquired with a PHI5000 VersaProbe II apparatus (ULVAC-PHI, Japan) equipped with an Al K_α anode (1486.6 eV); spectra were collected at high energy resolution (0.05 eV) using a 100 µm beam (25 W), collecting and analyzing in FAT mode electrons with a 45° take off angle, while compensating the electrical charging with both electrons and Ar^+ ions low energy beams.

Atomic Force Microscopy (AFM) was acquired in air with a Bruker FAST-SCANBIO microscope equipped with a closed-loop scanner (X, Y, Z maximum scan ranges: 35 mm, 35 mm, 3 mm, respectively). The scans were obtained in soft tapping mode in air, by using Bruker FASTSCAN-A probes with a nominal diameter of 5 nm. AFM images were obtained with a pixel resolution comparable to the tip size. The images were analyzed using Gwyddion 2.62.[27] Average roughness was evaluated over the full 5 × 5 µm image with the Otsu grain

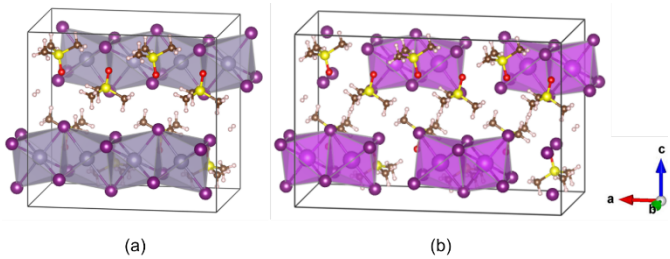

Fig. 1 (a) Undoped $TMSO_8Sn_8I_{24}$ 2 × 1 × 1 supercell. (b) $(TMSO)_3Bi_2I_9$ supercell. Iodine atoms are in violet, SnI_6 octahedra are in gray, BiI_6 octahedra in pink. Carbon, sulfur, oxygen, and hydrogen atoms are in brown, yellow, red, and white, respectively. The octahedral chains are aligned along the *a* direction.

marking algorithm. Scanning electron microscopy (SEM) was performed in secondary electron mode using a FEI Versa 3D microscope with 10 kV acceleration.

Results and discussion

The synthesis of the materials is a simple one-pot method (Scheme 1), using safe metals, unlike most perovskites that contain lead, and is conducted at room temperature except for a 10-minute step at 70 °C. The addition of (TMSO)I causes the immediate precipitation of the 1D perovskite, leading to single-phase polycrystalline specimens. For the sake of simplicity, in the following all samples are labeled according to the nominal fraction of bismuth used in the synthesis (Table S1), while the actual stoichiometry is described below. The substitution of Bi into $(TMSO)SnI_3$ is described using the quasi-chemical equation:

$$3Sn_{Sn}^{x} + 2BiI_3 \rightarrow 2Bi_{Sn}^{\bullet} + V_{Sn}'' + 3SnI_2 \quad (1)$$

On average, three Sn atoms are replaced by two Bi atoms, generating vacant cation sites (V_{Sn}''). Therefore, the solid solutions are best represented by the following formula: $(TMSO)_3Sn_{3x}Bi_{2(1-x)}I_9$ ($0 \le x \le 1$). For x = 1 and x = 0, this results in the all-tin ($TMSOSnI_3$) and all-bismuth ($(TMSO)_3Bi_2I_9$) end-member compositions, respectively. The intermediate compositions, formed by combining Bi^{3+} and Sn^{2+} in various molar ratios, exhibit structural isomorphism with the end members, all in agreement with the behavior previously described in detail for the related system $(TMSO)_3Pb_{3x}Bi_{2(1-x)}I_9$.[23,24,28,29]

The structure and possible arrangements of Sn/Bi/vacancies in the eight metal cation sites of a 2 × 1 × 1 supercell of these samples have been outlined in detail in our previous studies.[23,24,28] The only substantial change is the substitution of tin for lead, which, however, induces no difference from a structural point of view. XRD patterns, as shown in Fig. 2, reveal minor and predictable variations in peak positions as the material stoichiometry changes. As previously stated, increasing the concentration of bismuth results in a shrinkage of the unit cell along *a*. This causes a shift to higher angles for all *hkl* peaks

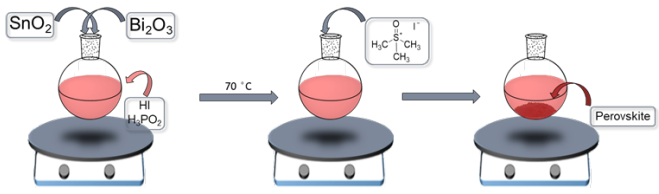

Scheme 1 Scheme of the synthesis of all samples.

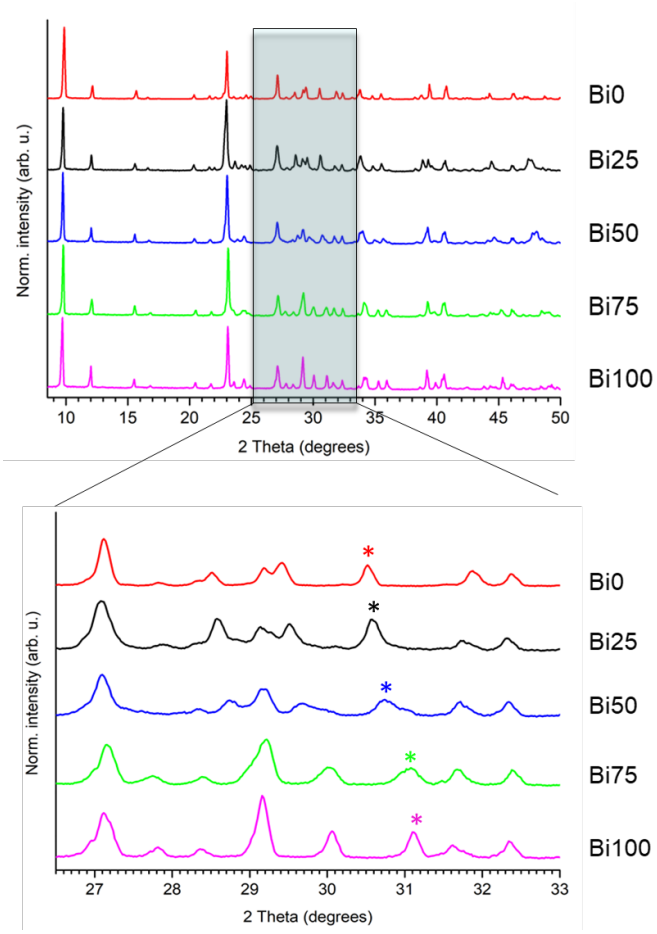

Fig. 2 XRD data of $(TMSO)SnI_3$, intermediate compositions $(TMSO)_3Sn_{3x}Bi_{2(1-x)}I_9$ ($0 \le x \le 1$), and $(TMSO)_3Bi_2I_9$ in the 8–50° 2θ range (bottom to top) with an enlargement of the 26–33° section, where the peak shift discussed in the text is marked with an asterisk.

with $h \neq 0$. In the inset of Fig. 2 it can be seen how the peak at 30.5° of **Bi0** (213 reflection), is shifted to the right as the concentration of bismuth increases, until it reaches a value of 31.1° in **Bi100**. For the same peaks with $h \neq 0$, a significant enlargement is observed, particularly in **Bi50** and **Bi75**, while the *0kl* peaks, unaffected by ordering or disorder within the Sn/Bi/V chains, keep their distinctive shape and position unchanged. The lattice parameters of all samples, shown in the Table 1, display distinctive trends in relation to the Bi/Sn ratio. Specifically, the *b* and *c* parameters, which are perpendicular to the metal halide chains, remain relatively unaffected by the extent of substitution. On the contrary, the *a* lattice parameter decreases linearly with increasing Bi content. This observation aligns with the nearly constant values of *b* and *c* lattice parameters, representing the cross-sectional dimensions of the polyanionic metal iodide chains. The relative ionic sizes and the presence of vacant sites contribute to

shrink the average periodicity along the *a* axis. By using the end-members as fixed points, the actual fraction of bismuth present in the solid solutions was calculated (Fig. 3) by interpolation. The independent assessment of the Bi/Sn stoichiometry from XRF agrees well with the one derived from the XRD lattice parameters, and the results are reported in Table 2. The experimental XANES spectra are shown in Fig. 4, and it is evident that Bi L_3-edge spectra of all samples are very different from reference BiI_3, and therefore, substantial decomposition to simple iodides from radiation damage can be reasonably excluded. In addition, there are no significant differences between the different spectra of the samples.

Table 1 Lattice parameters of all samples in the orthorhombic space group *Pnma*. Uncertainty is reported in parentheses.

SAMPLE	a (Å)	b (Å)	c (Å)	V (Å³)
Bi0	7.7631(3)	11.1739(4)	14.382(1)	1247.6(1)
Bi25	7.7040(4)	11.1815(8)	14.385(1)	1239.2(2)
Bi50	7.6431(7)	11.180(1)	14.375(3)	1228.5(3)
Bi75	7.5256(6)	11.213(1)	14.406(1)	1215.7(2)
Bi100	7.4534(4)	11.2149(6)	14.4017(8)	1203.8(1)

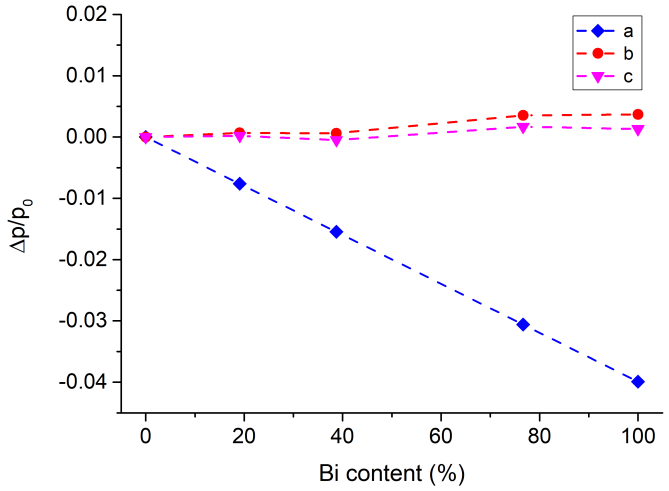

Fig. 3 Lattice parameter relative variation vs %Bi [Bi content (%)], in the form of $\Delta p/p_0$ (where p = a, b, c, and p_0 values are taken with reference to the $(TMSO)SnI_3$ species, that with x = 0) for the $(TMSO)_3Sn_{3x}Bi_{2(1-x)}I_9$ series. The uncertainty on $\Delta a/a_0$ is 10^{-4}.

Sn K-edge spectra are reported in Fig. 4a. All samples are similar to each other and very different from SnI_2, except for **Bi0**, whose edge is shifted to higher energy, evidencing a partial oxidation of tin(II) to tin(IV) leading to SnO_2 which is also confirmed through the EXAFS analysis reported below. This was likely triggered by the primary beam, assisted probably by trace moisture in the boron nitride dilutant. Such process only occurs in the bismuth-free sample,

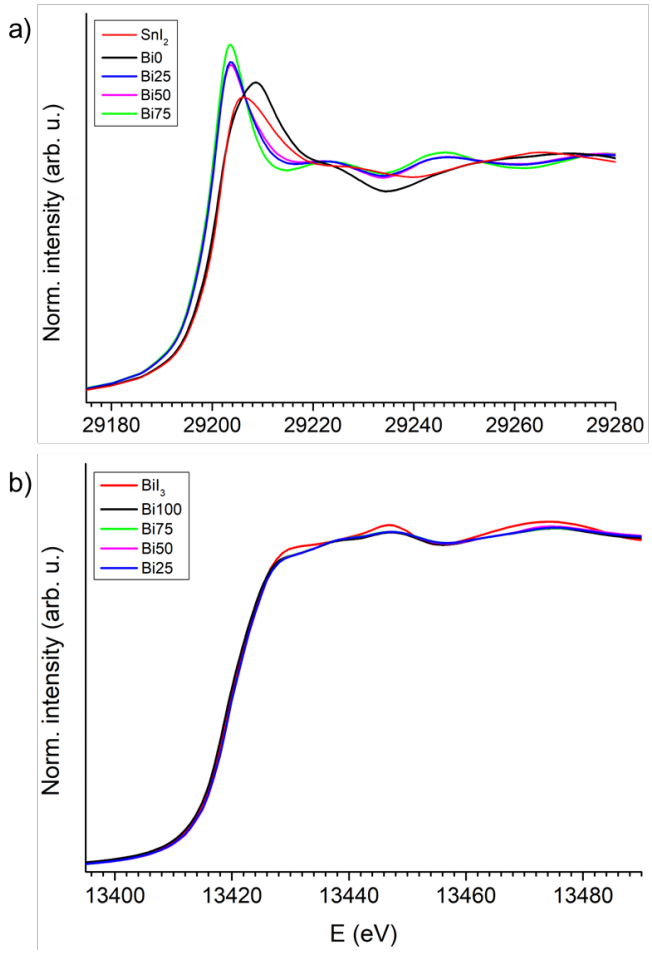

Fig. 4 (a) Sn K-edge and (b) Bi L_3-edge spectra for all samples, compared with the respective simple metal iodide.

Table 2 x values for the intermediate compositions $(TMSO)_3Sn_{3x}Bi_{2(1-x)}I_9$ formula, obtained from XRD and XRF respectively.

	XRD			XRF		
SAMPLE	x	%Bi	Formula	x	%Bi	Formula
Bi25	0.81	19	$(TMSO)_3Sn_{2.42}Bi_{0.38}I_9$	0.82	18	$(TMSO)_3Sn_{2.46}Bi_{0.36}I_9$
Bi50	0.61	39	$(TMSO)_3Sn_{1.84}Bi_{0.77}I_9$	0.57	43	$(TMSO)_3Sn_{1.71}Bi_{0.86}I_9$
Bi75	0.23	77	$(TMSO)_3Sn_{0.69}Bi_{1.54}I_9$	0.24	76	$(TMSO)_3Sn_{0.72}Bi_{1.52}I_9$

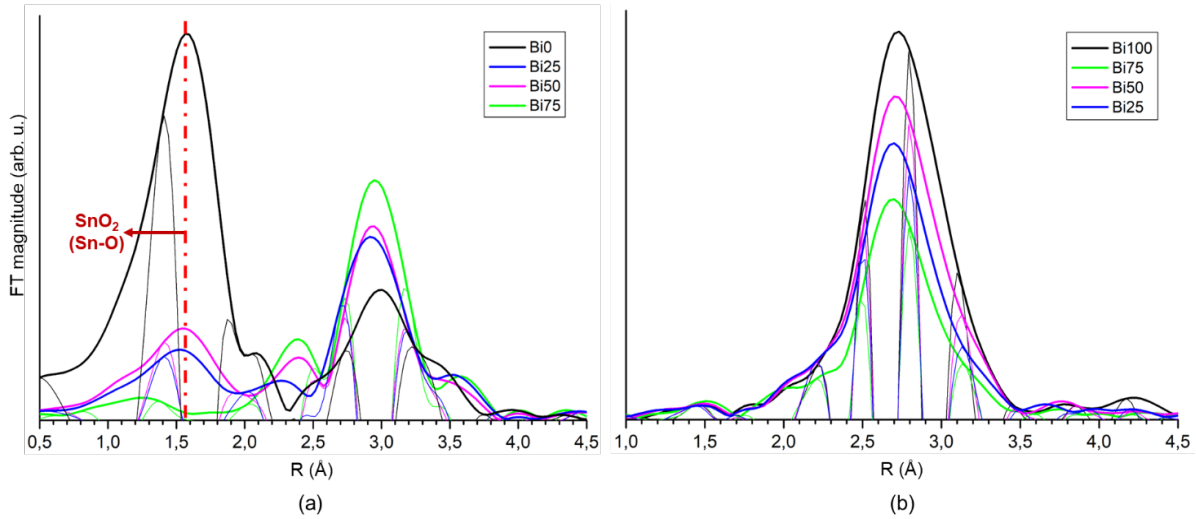

Fig. 5 Fourier-transformed EXAFS spectra of samples at the (a) Sn K-edge and (b) Bi L_3-edge. The Sn-O signal assigned to the formation of SnO_2 is marked with a red line.

while the other samples do not show significant oxidation. Looking deeper into the matter from the EXAFS spectra (Fig. 5), there is indeed a very large Sn-O signal attributable to SnO_2 in **Bi0**, which dramatically decreases as the concentration of bismuth increases, all but disappearing in **Bi75**. This suggests that bismuth protects tin(II) from photooxidation to tin(IV). Further confirmation of tin oxidation in sample **Bi0** and the absence of this phenomenon in sample **Bi75** is provided by XRD patterns recorded before and after exposure to the synchrotron beam (Fig. S6): the diffractogram of **Bi75** after exposure found before exposure, keeping positions unchanged, confirming that the sample did not undergo oxidation upon exposure to the X-ray beam. In order to understand if any modifications occurred after thin film deposition, XPS spectra of the freshly deposed film were collected. Fig. 6 shows an example for **Bi75** sample in the Bi 4f region. It is possible to observe a conspicuous reduction (ca. 23%) of Bi(III) to Bi(0); and, most interestingly, the strongly asymmetric line shape of Bi(0) suggests an extensive electron delocalization, suggesting the presence of a metallic bond between Bi(0) atoms. It is worth noticing that, even if previous papers reported such an effect as a consequence of X-ray exposition,[30,31] this is not our case: powdered samples of all prepared perovskites were exposed to the same radiation (Al Kα, 1486.6 eV) for twice the time used to acquire the film sample spectrum, and no reduction effects whatsoever were observed, for all samples. It is therefore also possible to attribute reduction to the solution/suspension process[31]. The UV-vis-NIR reflectance spectra of all samples as bulk powder (Fig. S7) show well-

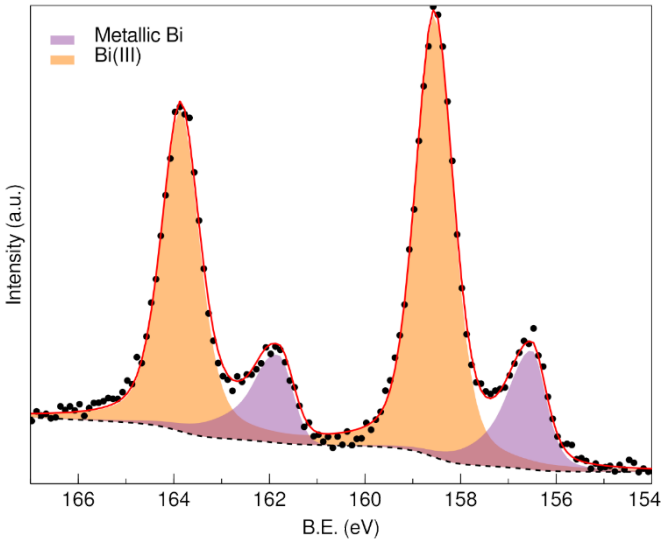

Fig. 6 XPS spectrum of Bi75 in the Bi 4f region.

specific trends, except for $(TMSO)_3Bi_2I_9$ (sample **Bi100**). At about 350 nm, an increase in percent diffuse reflectance is appreciated in agreement with the amount of bismuth in the material. The optical band gap (Eg) values, for each sample, were experimentally obtained from Tauc plots, summarized in Fig. S8. The band gap follows a U-shaped curve with increasing bismuth content (Fig. 7), with a steady decrease of the band gap except for $(TMSO)_3Bi_2I_9$ (sample **Bi100**). This trend mirrors what was observe in our previous work [23] for Pb/Bi compositions, with a further decrease in band gaps: in particular, the minimum band gap obtained with tin is 1.96 eV for **Bi75**.[23]

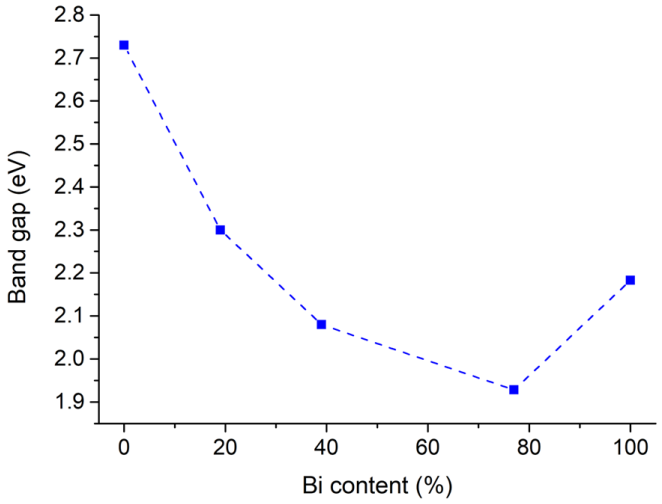

Fig. 7 Optical band gap of bulk powders as a function of %Bi.

Electrical Properties and Piezoresistivity

The flexible substrates were mounted on a 3D-printed foldable device (Fig. S9) with one end fixed, allowing bending at different angles (0°, 30°, 60°, 90°) with a bending radius of 10 mm, for the acquisition of I-V curves (Fig. 8). A first analysis reveals that the initial bending step (0-30°) results in a decrease in current slope for all the samples. Specifically, the ITO control sample shows a current variation of approximately 1.66 mA, while the **Bi50** and **Bi100** samples exhibit relatively minor current changes (0.32 and 0.78 mA, respectively). In contrast, the remaining samples show more significant variations, with **Bi0**, **Bi25**, and **Bi75** experiencing changes of 3.38, 4.72, and 2.97 mA, respectively. In the bending range between 30 and 90°, the ITO sample displays a current variation of approximately 1 mA for each step, whereas **Bi25** shows no significant variations, despite having the largest initial current change. **Bi0**, on the other hand, exhibits changes of about 1.2 mA for each step, slightly higher than the control. **Bi75** maintains a 3 mA variation in the second bending step, which subsequently increases to 3.68 mA in the final bending step, demonstrating tripled sensitivity compared to the substrate alone. A rigorous statistical analysis, based on the average of 16 different scans, was then conducted to assess the decrease in current values measured at +2 V (Fig. 9). The diverse electrical responses can be attributed to both the varying bismuth concentration and the different morphology and roughness of the films. Indeed, the gauge factors for bending at the different bismuth concentration were calculated as (ΔR/R)/ε where ε, Δ*R*, and *R* are the strain applied to the sensor, resistance variation at ε strain, and initial resistance at zero strain, respectively.[32] The strain can be estimated

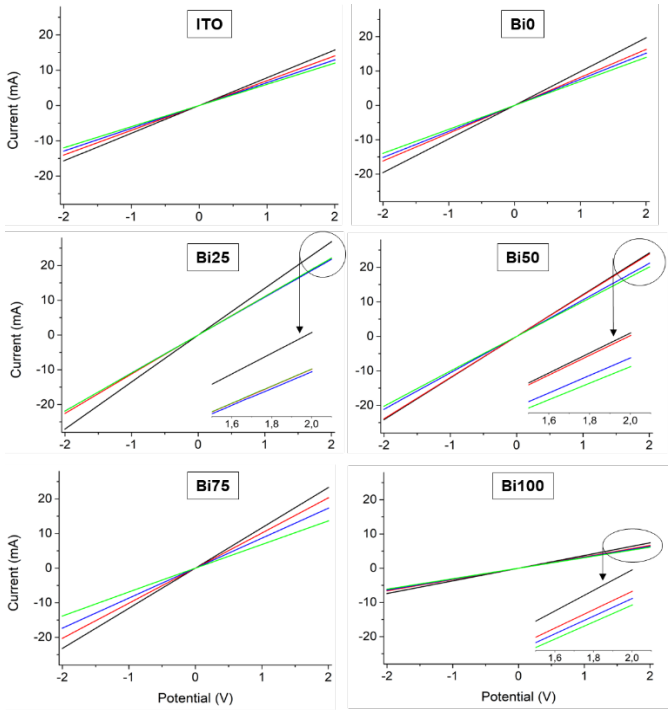

Fig. 8 *I-V* characteristic curves at different bending angles: 0° (black lines), 30° (red lines), 60° (blue lines), 90° (light green lines). The insets highlight subtle differences among the various bending angles, otherwise scarcely perceptible.

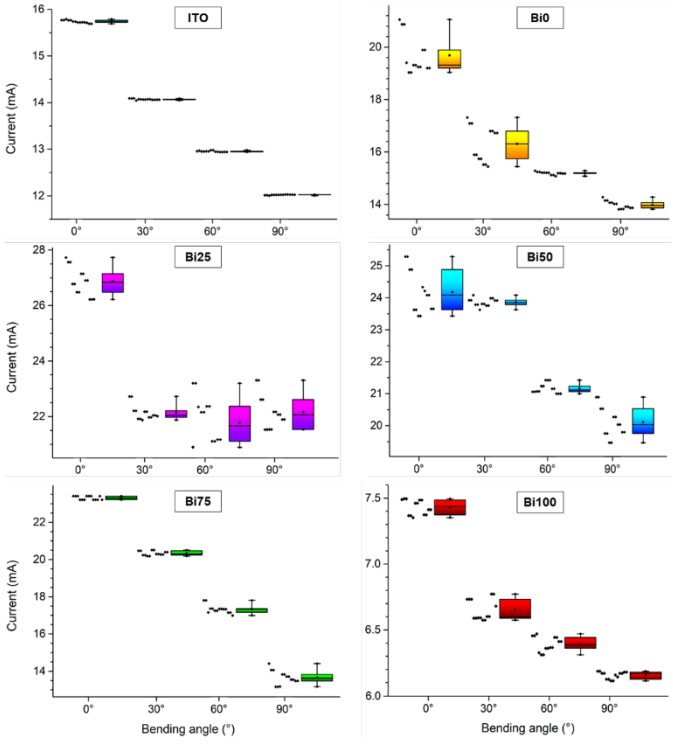

Fig. 9 Statistical box plots of the fourteen measured current values along with their average at +2 V voltage bias for the ITO/PET substrate and for all samples.

by the equation ε = h/2R, where *h* is the ITO/PET thickness of the substrate (about 150 µm) and *R* is the bending radius, equal to 16, 14, and 12 mm for bending angles of 30°, 60°, and 90°, respectively.

The highest value of ~70 was observed for **Bi75** and **Bi100** to be compared with the **Bi0**, **Bi25** and **Bi50** and ITO control samples that all showed lower gauge factor values, equal to 50, 24, 13 and 40, respectively. Notably, **Bi100** showed an almost constant gauge factor at all the different bending strains, whereas **Bi75** reached a value as high as 110 at 90° bending. The most promising sample, **Bi75**, underwent a series of multiple bending tests from 0 to 90° (Fig. S10) to evaluate the repeatability and durability of the sensor under repeated stress conditions. The sensor demonstrated excellent long-term repeatability, confirming its suitability as a suitable candidate for this type of device.

Thin Films Morphology

The AFM imaging shows how the morphology of the film undergoes significant changes with different bismuth concentration. In particular, **Bi0** (Fig. 10a) exhibits a peculiar grain shape, entirely different from the other compositions. **Bi0** does not display good grain compactness and has a relatively high average roughness of 8.98 nm. Nevertheless, the I-V curves and the calculated gauge factor showed slightly better results than the ITO control. This can be explained by the fact that the film has an average grain size of 150 nm with a well-defined orientation, helping the grains move apart when bent, reducing the current, and then returning to their original position. In contrast, the **Bi25**, **Bi50**, and **Bi100** samples did not yield positive responses in the I-V curves. **Bi25** (Fig. 10b), despite having a lower average roughness (4.75 nm) compared to **Bi0**, has a smaller average grain size of about 88.91 nm, and their distribution is rather discontinuous. **Bi50** (Fig. 10c), on the other hand, has a more compact and continuous grain distribution with an average size, equal to 93.74 nm, but it exhibits a higher average roughness of 9.22 nm. **Bi100** (Fig. 10f) presents the least favorable conditions for good electrical conduction, as it has the smallest average grain size, about 66 nm, a discontinuous grain distribution, and an average roughness of 8.2 nm. **Bi75** (Fig. 10d-e) displays a rather unique morphology. The film consists of very compact grains that are not easily distinguishable, leading to an extremely dense and continuous distribution, with distinctive tips about 8-12 nm. In this case, it is difficult to estimate the average grain size due to the compactness of the film. Despite the presence of these peaks, the film keeps an extremely low roughness of 0.86 nm. Thus, the dense, compact, and continuous grain network combined with the low roughness explains why this sample performs better than others. The SEM analysis reveals the morphological difference of the **Bi75** sensor before and after bending (Fig. 11). Considering that the sample exhibits a dense, uninterrupted network of grains, bending in this case, probably does not result in their separation, but rather causes them to slide. Once the device is returned to its resting state, this sliding leads to the formation of raised microstructures which are extremely oriented, all parallel to each other. Indeed, the presence of sliding conductive networks has already been studied in previous piezoresistive sensors that introduced lubricants such as fullerene[30] or MoS_2 [31] particles, resulting in a significative enhancement of piezosensing performances with respect to films without lubricity. Once the device is returned to its resting state, this sliding leads to the formation of oriented raised microstructures, all parallel to each other. The direction of strain is approximately parallel to the direction at which the bending strain is applied.

EIS characterization was carried out on the Bi75 sample before and after the application of the bending strain. The sample before the bending strain showed an almost totally resistive response (Fig. 12a), resulting in a model circuit (χ^2= 0.0012) with a resistance (R_{film}) with of 294 ± 2 Ω, hinting to a current flow through unperturbed resistive paths. The EIS analysis on the sample after the 0°-90°-0° bending cycles shows a significant increase of the total impedance of the system in the imaginary component as well. This results in an electrical model in which a resistance is put in parallel to a capacitance (circuit 1, χ^2= 0.005, see Fig. 12b), or to a pseudo-capacitance (circuit 2, χ^2 = 0.004, see Fig. S11), also defined as constant phase element (CPE). The impedance of a CPE is described by:

$$\frac{1}{Q_0 \omega^n} e^{-\frac{\pi}{2} n i}$$

where Q_0=1/|Z| and 0<n<1. These two circuits however provide results which are not statistically different. Indeed, the resistance of the film after the bending strain (R_{film}') is 36.7 kΩ (±0.01%) for circuit 1 and 36.8 kΩ (±0.01%) for circuit 2. The capacitance value of 3.1 pF (±1.5%) is found for circuit 1, whereas a pseudo impedance of the CPE equal to 4.6 pF (±13.4%) and n = 0,973 (±0.95%) is found for circuit 2. To further ensure the stability, linearity and casualty of both EIS data, a satisfactory Kramers-Kroning test was also performed.

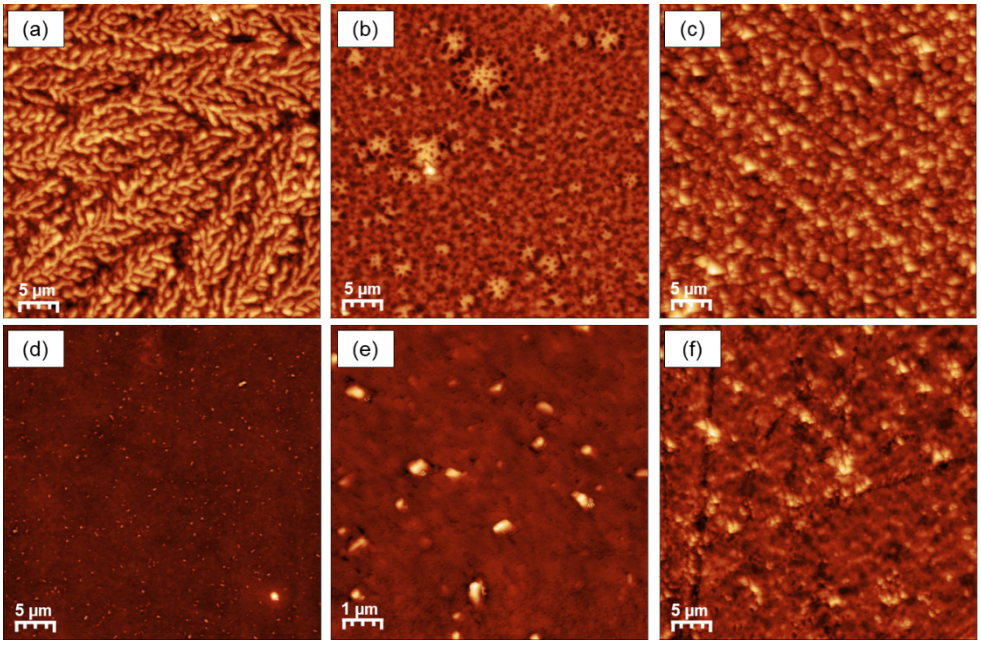

Fig. 10 AFM top images of (a) Bi0, (b) Bi25, (c) Bi50, (d) Bi75, (e) enlargement of Bi75, (f) Bi100.

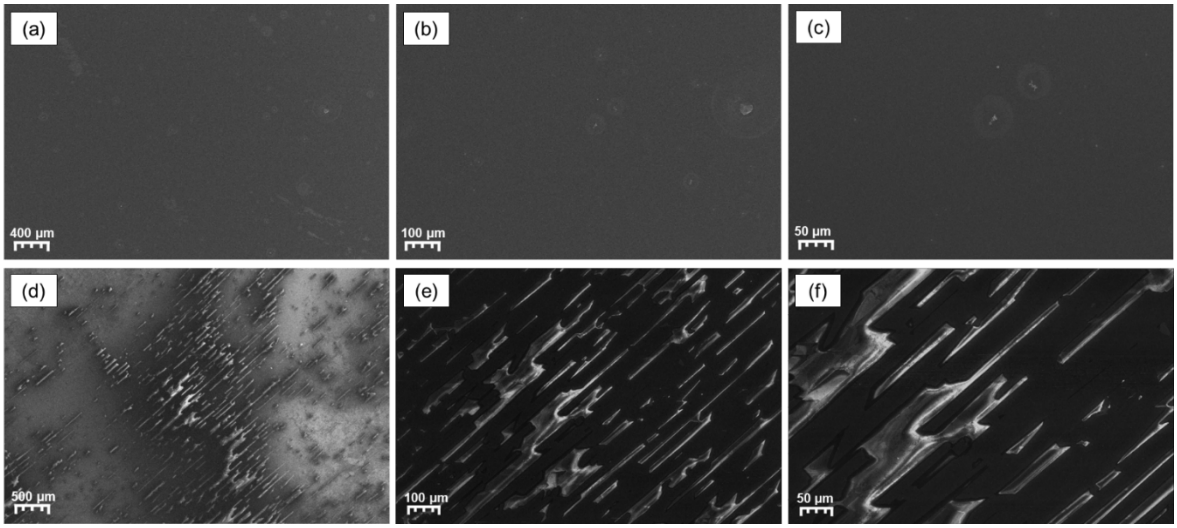

Fig. 11 Top-view SEM images of (a-c) Bi75 before bending, (d-f) Bi75 after bending.

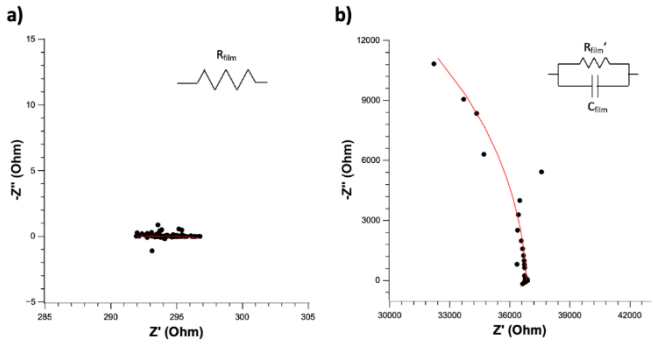

Fig. 12 Nyquist plots and relative fits of Bi75 bending sensors (a) before and (b) after 0°-90°-0° bending cycles. The best fits for model circuits are reported as red solid lines in the respective legends.

- i.e. $\chi^2 < 10^{-5}$ for the pristine **Bi75** sample and $\chi^2 < 10^{-4}$ for the stressed sample. Accordingly, these values well agree with a picture in which the perovskite is affected by defect propagation after the bending stress, leading to microcracks and delamination at the microscale as shown by SEM characterization. These microscale defects concentrate charge carriers in solid films in accordance with previous EIS models,[32] ultimately reducing the overall conductivity of the films after the application of bending stress.

Conclusions

This work shows the synthesis of a novel lead-free hybrid organic-inorganic perovskite $(TMSO)_3Sn_3xBi_{2(1-x)}I_9$ ($0 \leq x \leq 1$) formed by combining Bi^{3+} and Sn^{2+} in different ratio. The Bi^{3+} dependent piezoresistivity of the thin films grown on ITO/PET flexible supports is studied as a function of the Bi^{3+} concentration. Bi^{3+} induces the formation of vacant cation sites in the crystalline cell, leading to shrinkage of the crystalline cell along the *a* axis. This control of the cell size is the key to guide the control of the thin film morphology from separated grains to compact, dense features that are piezo-responsive. The films produced with low amount or no Bi^{3+} display piezoresistive properties similar or even worse than the ITO control, while when Bi^{3+} is the predominant metal ion, the corresponding piezoresistive features are improved. An optimal composition is found in Bi75, at which the perovskite bandgap can be lowered to 1.96 eV, and the gauge factor improves by increasing the bending strain, from 30 to 62 and 110 at 0.4%, 0.5% and 0.6% strains, respectively. This composition shows an almost flat surface with compact grains and vertical tips, which under the application of bending strain is expected to produce sliding of the grains and film delamination, as confirmed by SEM. These observations can be explained by considering that the sliding grains piezoresistive mechanism likely observed in Bi75 resembles the one observed in graphene conductive networks, where fullerene[33] or MoS_2[34] lubricant particles increase strain sensitivity at higher ranges with respect to films without lubricity by favouring film sliding. On the contrary, all the other perovskite compositions show nanoscale grains. Indeed, perovskite films containing only Bi^{3+} and no Sn^{2+} show a discontinuous grain distribution, resulting in a surprising constant gauge factor around 65 at all the investigated bending strains which is significantly better than the control ITO, especially at small bending angles. Such constant response of the perovskite containing only Bi^{3+} and no Sn^{2+} can be due to the bending induced separation of grains which is known to produce an increase in relative resistance R/R_0 change of the film in accord with physical models used for conductor-filled polymer composites. [18] This study shows a first step towards the tailored design of a lead-free halide perovskite where the introduction of bismuth ions triggers unprecedented piezoresistive properties to prepare bending sensors requiring sensitivity to small and high bending angles, which can find applications for wearable electronics and soft robotics.

Author Contributions

Methodology, formal analysis: S.V., G.A., V.F., M.S., A.L.
Supervision, Conceptualization, Funding acquisition: B.P., F.G.
Writing – original draft: S.V., G.A. Writing – review&editing: F.G.

Conflicts of interest

There are no conflicts to declare.

Acknowledgements

The authors acknowledge beamtime provision from the European Synchrotron Radiation Facility (proposal MA-5465) and thank J. Orsilli for assistance during the experiments. The ATeN Center (Università di Palermo) is acknowledged for assistance and service. Partial financial support from MUR is acknowledged under grants PRIN2022 “Novel SUstainable double PERovskites: multiscale characterization from the atomic structure to functional properties (SU-PER)”, “Network 4 Energy Sustainable Transition – NEST” B73C22001280006 (project funded under the National Recovery and Resilience Plan (NRRP), Mission 4 Component 2 Investment 1.3–funded by the European Union – NextGenerationEU) and “SiciliAn MicronanOTecH Research And Innovation CEnter "SAMOTHRACE" (MUR, PNRR-M4C2, ECS_00000022), spoke 3 - Università degli Studi di Palermo "S2-COMMs - Micro and Nanotechnologies for Smart & Sustainable Communities".

References

1 G. Giuliano, A. Bonasera, G. Arrabito and B. Pignataro, *Sol. RRL*, 2021, **5**, 12.
2 H. Liu, X. Zhang, L. Zhang, Z. Yin, D. Wang, J. Meng, Q. Jiang, Y. Wang and J. You, *J. Mater. Chem. C*, 2017, **5**, 6115–6122.
3 K. Lin, J. Xing, L. N. Quan, F. P. G. de Arquer, X. Gong, J. Lu, L. Xie, W. Zhao, D. Zhang, C. Yan, W. Li, X. Liu, Y. Lu, J. Kirman, E. H. Sargent, Q. Xiong and Z. Wei, *Nature*, 2018, **562**, 245–248.
4 D. Bin Kim, K. H. Park and Y. S. Cho, *Energy Environ. Sci.*, 2020, **13**, 2077–2086.
5 S. Körbel, M. A. L. Marques and S. Botti, *J. Mater. Chem. C*, 2016, **4**, 3157–3167.
6 M. Budimir, D. Damjanovic and N. Setter, *Phys. Rev. B*, 2006, **73**, 174106.
7 M. H. Lee, D. J. Kim, J. S. Park, S. W. Kim, T. K. Song, M. H. Kim, W. J. Kim, D. Do and I. K. Jeong, *Adv. Mater.*, 2015, **27**, 6976–6982.
8 Y. Kuroiwa, S. Kim, I. Fujii, S. Ueno, Y. Nakahira, C. Moriyoshi, Y. Sato and S. Wada, *Commun. Mater.*, 2020, **1**, 71.
9 H. Park, C. Ha and J. H. Lee, *J. Mater. Chem. A*, 2020, **8**, 24353–24367.
10 M. Coll, A. Gomez, E. Mas-Marza, O. Almora, G. Garcia-Belmonte, M. Campoy-Quiles and J. Bisquert, *J. Phys.*

Chem. Lett., 2015, **6**, 1408–1413.
11 X.-G. Chen, X.-J. Song, Z.-X. Zhang, P.-F. Li, J.-Z. Ge, Y.-Y. Tang, J.-X. Gao, W.-Y. Zhang, D.-W. Fu, Y.-M. You and R.-G. Xiong, *J. Am. Chem. Soc.*, 2020, **142**, 1077–1082.
12 H. S. Wu, B. T. Murti, J. Singh, P. K. Yang and M. L. Tsai, *Adv. Sci.*, 2022, **9**, 1–13.
13 H.-Y. Ye, Y.-Y. Tang, P.-F. Li, W.-Q. Liao, J.-X. Gao, X.-N. Hua, H. Cai, P.-P. Shi, Y.-M. You and R.-G. Xiong, *Science (80-.).*, 2018, **361**, 151–155.
14 H. Zhang, Z.-K. Xu, Z.-X. Wang, H. Yu, H.-P. Lv, P.-F. Li, W.-Q. Liao and R.-G. Xiong, *J. Am. Chem. Soc.*, 2023, **145**, 4892–4899.
15 S. Ippili, V. Jella, S. Eom, S. Hong and S.-G. Yoon, *ACS Appl. Mater. Interfaces*, 2020, **12**, 50472–50483.
16 S. Mondal, S. Maiti, T. Paul, A. Sahoo, S. Bhattacharjee, N. S. Das and K. K. Chattopadhyay, *Appl. Mater. Today*, 2022, **26**, 101385.
17 J. Han, D. Bin Kim, J. H. Kim, S. W. Kim, B. U. Ahn and Y. S. Cho, *Nano Energy*, 2022, **99**, 107421.
18 X. Zhang, Y. I. Pan, Q. Zheng and X. Yi, *J. Polym. Sci. B Polym. Phys.*, 2000, **38**, 2739–2749.
19 H. Zhang, X. Fu, Y. Tang, H. Wang, C. Zhang, W. W. Yu, X. Wang, Y. Zhang and M. Xiao, *Nat. Commun.*, 2019, **10**, 1088.
20 Y. Zhuang, L. Cao, X. Gu, S. Miao, S. Gao, Y. Fang, S. Huang and X. He, *Ceram. Int.*, 2024, **50**, 5766–5774.
21 S. Mondal, S. Poddar, S. Bhattacharjee, S. Maiti, A. Banerjee and K. K. Chattopadhyay, *Nano Energy*, 2023, **115**, 108689.
22 D. R. Baer and S. Thevuthasan, *Characterization of Thin Films and Coatings*, Elsevier Ltd., Third Edit., 2009.
23 C. Pipitone, F. Giannici, A. Martorana, G. García-Espejo, S. Carlotto, M. Casarin, A. Guagliardi and N. Masciocchi, *J. Phys. Chem. C*, 2021, **125**, 11728–11742.
24 S. Virga, A. Longo, C. Pipitone and F. Giannici, *J. Phys. Chem. C*, 2023, **127**, 18058–18066.
25 B. H. Toby and R. B. Von Dreele, *J. Appl. Crystallogr.*, 2013, **46**, 544–549.
26 B. Ravel and M. Newville, *J. Synchrotron Radiat.*, 2005, **12**, 537–541.
27 D. Nečas and P. Klapetek, *Open Phys.*, 2012, **10**, 181–188.
28 C. Pipitone, S. Carlotto, M. Casarin, A. Longo, A. Martorana and F. Giannici, *J. Mater. Chem. C*, 2022, **10**, 1458–1469.
29 C. Pipitone, F. Ursi, F. Giannici, A. Longo, A. Guagliardi, N. Masciocchi and A. Martorana, *Nanotechnology*, 2022, **33**, 425703.
30 Ş. Süzer, *Appl. Spectrosc.*, 2000, **54**, 1716–1718.
31 H. Zhao, K. Chordiya, P. Leukkunen, A. Popov, M. Upadhyay Kahaly, K. Kordas and S. Ojala, *Nano Res.*, 2021, **14**, 1116–1125.
32 J. Soares Costa, M. Prestat, B. Tribollet, B. Lescop, S. Rioual, L. Holzer and D. Thierry, *ChemElectroChem*, 2020, **7**, 2055–2064.
33 X. Shi, S. Liu, Y. Sun, J. Liang and Y. Chen, *Adv. Funct. Mater.*, 2018, **28**, 1–10.
34 H. Wang, J. Liu, H. Cui, Y. Liu, J. Zhu, H. Wang, G. Song, Z. Li and D. Chen, *ACS Appl. Electron. Mater.*, 2021, **3**, 1758–1770.